sensors

MDPI

Review

Reduced Graphene Oxide (rGO)-Loaded Metal-Oxide Nanofiber Gas Sensors: An Overview

Sanjit Manohar Majhi [1,2,†], Ali Mirzaei [3,†], Hyoun Woo Kim [1,2] and Sang Sub Kim [4,*]

[1] Division of Materials Science and Engineering, Hanyang University, Seoul 04763, Korea; sanjit.majhi@kaust.edu.sa (S.M.M.); hyounwoo@hanyang.ac.kr (H.W.K.)
[2] The Research Institute of Industrial Science, Hanyang University, Seoul 04763, Korea
[3] Department of Materials Science and Engineering, Shiraz University of Technology, Shiraz 71557-13876, Iran; Mirzaei@sutech.ac.ir
[4] Department of Materials Science and Engineering, Inha University, Incheon 22212, Korea
* Correspondence: sangsub@inha.ac.kr
† These authors contributed equally to this work.

Abstract: Reduced graphene oxide (rGO) is a reduced form of graphene oxide used extensively in gas sensing applications. On the other hand, in its pristine form, graphene has shortages and is generally utilized in combination with other metal oxides to improve gas sensing capabilities. There are different ways of adding rGO to different metal oxides with various morphologies. This study focuses on rGO-loaded metal oxide nanofiber (NF) synthesized using an electrospinning method. Different amounts of rGO were added to the metal oxide precursors, and after electrospinning, the gas response is enhanced through different sensing mechanisms. This review paper discusses rGO-loaded metal oxide NFs gas sensors.

Keywords: gas sensor; reduced graphene oxide; rGO-loading; metal oxide; sensing mechanism

Citation: Majhi, S.M.; Mirzaei, A.; Kim, H.W.; Kim, S.S. Reduced Graphene Oxide (rGO)-Loaded Metal-Oxide Nanofiber Gas Sensors: An Overview. *Sensors* **2021**, *21*, 1352. https://doi.org/10.3390/s21041352

Academic Editor: Eduard Llobet
Received: 26 December 2020
Accepted: 10 February 2021
Published: 14 February 2021

1. Introduction

Metal oxide gas sensors are used to sense various toxic gases and vapors [1,2] in many areas [3]. These sensors are quite popular owing to their low preparation costs, high sensitivity, fast dynamics, high stability, simple operation, and small size [4]. The general gas sensing mechanism of metal oxide gas sensors stems from the modulation of electrical resistance in the presence of target gases [5]. In these sensors, the sensing layer is exposed directly to the gas. The interaction between the target gas and sensing layer modulates the electrical resistance of the gas sensor, resulting in the generation of a sensing signal. This conductivity change is due to variations in the width of the electron depletion layer across the exposed area of the sensing layer [6]. Various strategies can be used to enhance the gas sensing characteristics of metal oxide-based gas sensors, such as UV light activation [7], fabrication of p-n, p-p and n-n heterojunctions [8], noble metal decoration [9],surface engineering, and the generation of structural defects [10]. Thus far, different morphologies of metal oxides, such as nanowires [11], nanotubes [12], nanorods [13], nanobelts [14], nanofibers (NFs), nanosheets [15], and hierarchical structures [16], have been used in gas sensing studies. This is because gas adsorption on the surface of gas sensing relates directly to the surface area of gas sensors and higher adsorption of gas means higher sensing signal. Thus, several studies have attempted to synthesize morphologies with a high surface area to increase the sensing performance of gas sensors. In addition, a porous morphology [17] and hollow structures [18,19] can be other useful techniques to increase the gas sensing properties. Therefore, metal oxide NFs are highly popular for sensing studies because of a very high surface area results from the one-dimensional morphology and the presence of nanograins on their surfaces, as shown in Figure 1. The generation of depletion layers on nanograins causes the development of potential barriers, which will be modulated during exposure to the target gases, contributing to the sensing signal generation.

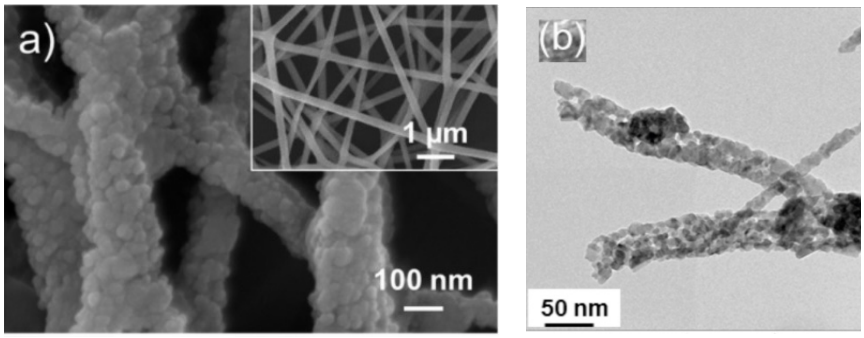

Figure 1. (**a**) FE-SEM image of ZnO electrospun NFs. The inset indicates high magnification image [20] (**b**) TEM image of 0.5 SnO_2–0.5 Co_3O_4composite NFs [21].

Another advantage of NFs is their ease of preparation using a facile electrospinning technique. In general, the electrospinning technique can be used to fabricate continuous fibers with the possibility of control over the fiber diameter [22]. In addition, different NFs, such as porous NFs [23], core-shell NFs [24,25], and complex NFs [26], can be easily synthesized by electrospinning. Furthermore, NFs with controllable alignment can be produced by modifying the electrospinning [27]. Electrospinning also can be used for the mass production of NFs because of the easy handling, possibility of control of the diameter, low cost, simple operation, and high reproducibility [28]. Briefly, the features of electrospun fibers can be controlled by electrospinning parameters, including the solution variables (e.g., surface tension, viscosity, and conductivity), operating variables (e.g., applied voltage, spinning distance, and solution flow rate), and ambient variables (e.g., humidity and temperature) [29].Li et al. [30] (Figure 2) and Xue et al. [31] reviewed these factors, so this review paper does not discuss them further.

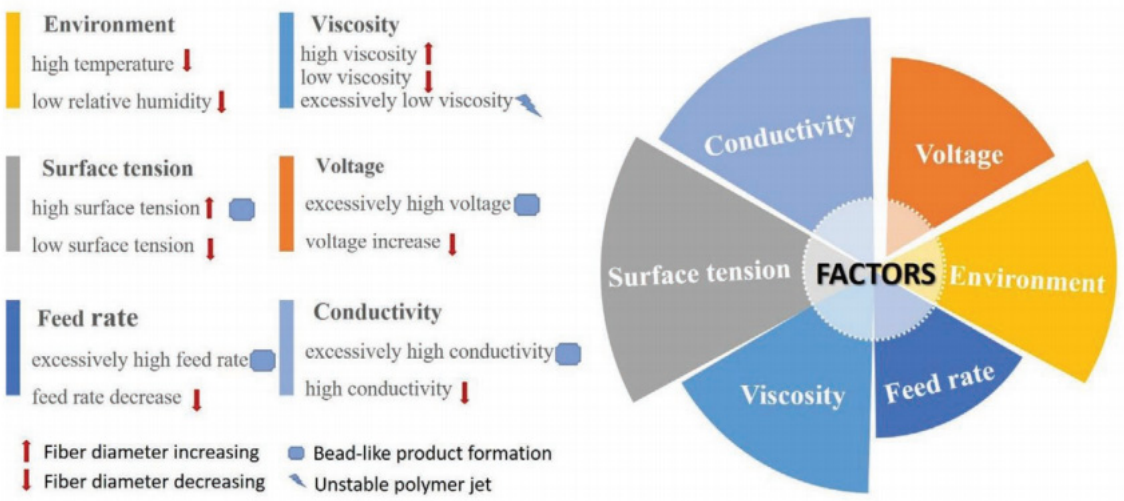

Figure 2. Factors affecting fiber formation during electrospinning [30].

Figure 3 shows the major components of electrospinning include a syringe pump, spinneret, conductive collector, and power supply. The electrospinning technique can be described as follows: (1) charging of the liquid droplet and the formation of a Taylor cone, (2) formation of the charged jet, (3) thinning of the jet by the applied voltage, and (4) collection and solidification of the jet on a grounded collector. A Taylor cone is formed owing to surface tension and the applied electric field, from which a charged jet is ejected. The ejected jet was solidified quickly, resulting in the collection of solid fibers on the collector [32,33].

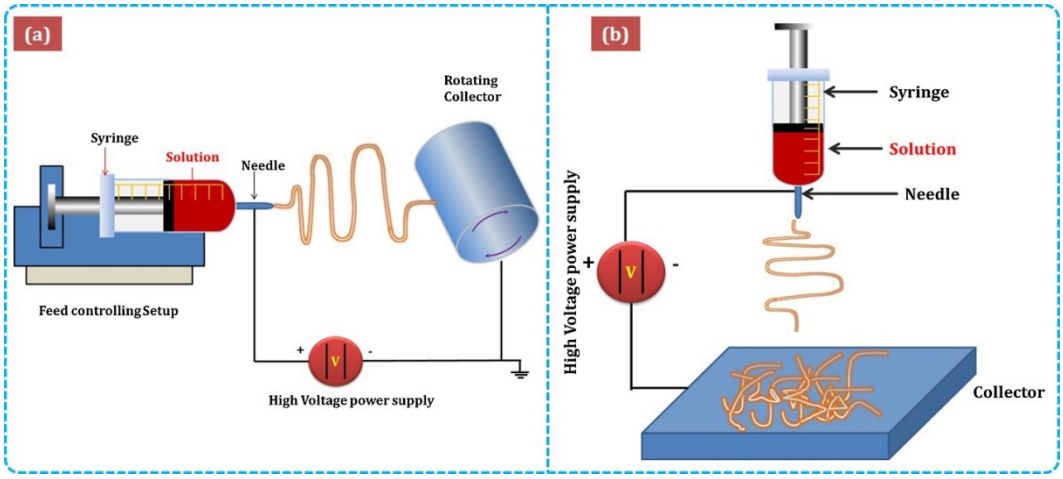

Figure 3. Schematic diagram of (**a**)horizontal and(**b**)vertical setups of electrospinning [34].

2. Graphene, Graphene Oxide, and Reduced Graphene Oxide

Graphene is a single-layer comprised of sp^2carbon atoms that can be used as a gas sensor owing to its high charge carrier mobility (200,000 cm^2 V^{-1} s^{-1}), high mechanical stiffness, high environmental compatibility, and huge surface area (2630 m^2g^{-1}) [35,36]. Schedin et al. [37] introduced the first graphene gas sensor in 2007. Because atoms in a single layer of graphene can be considered surface atoms, graphene can interact with even a single molecule [37]. Even though nowadays pristine graphene can be synthesized on a large scale [38] with good water solubility [39,40], it can be easily agglomerated in solution due to surface interactions [41]. Moreover, graphene has no bandgap or functional groups, limiting its gas sensors applications, particularly in the pristine form [42]. Therefore, reduced graphene oxide (rGO), which is synthesized by the reduction of graphene oxide (GO), is a better choice for gas sensing applications because it has many functional groups and defects [43]. GO has also been used for gas sensing studies [44]. On the other hand, GO has very high resistance due to the presence of alkoxy (C-O-C), hydroxyl (-OH), carboxylic acid (-COOH), carbonyl (C=O), and other oxygen-based functional groups [45,46]. rGO has more defects and dangling bonds than graphite, resulting in better sensing properties [47]. GO is widely prepared using either Hummers [48] or Brodie [49] methods. In these methods, differences are in both the acid used (nitric or sulfuric acid), and the type of salt used (potassium chlorate or potassium permanganate). By subsequent reduction of GO, rGO can be obtained. In fact, rGO can be prepared easily from GO by chemical reduction, thermal reduction, and UV light reduction [50]. Figure 4 shows the structure and preparation of GO and rGO [44].

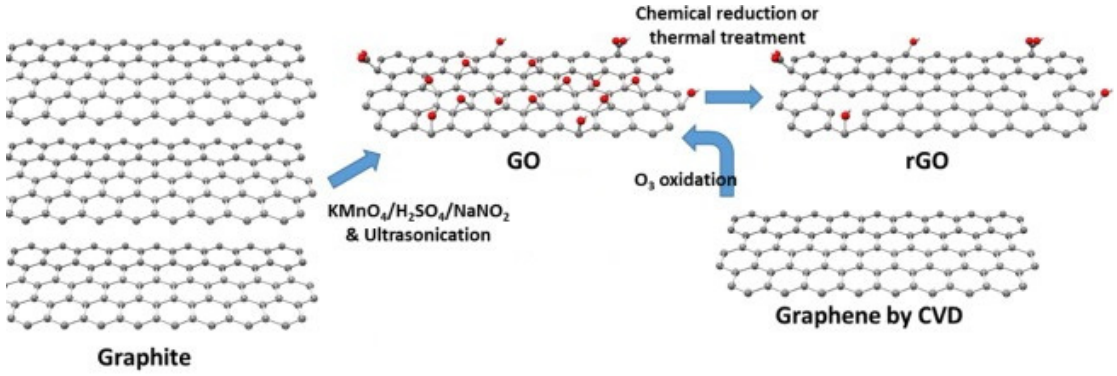

Figure 4. Structure and preparation of GO and rGO [44].

Furthermore, rGO has high thermal stability, and the total weight loss of rGO was reported to be only 11% up to 800 °C, which was attributed to the absence of most oxygen functional groups. [51]. Pristine rGO gas sensors have a long response and recovery times, and incorporating rGO with metal oxides can be a good strategy to increase the sensing capabilities of rGO-based gas sensors [52]. The synthesis and properties of rGO have been reviewed comprehensively [41]. The following section explains the gas sensing capability of rGO-loaded metal oxide NFs. This paper does not discuss the combination of rGO with other materials, such as mesh fabric [53] or polymers [54,55], for gas sensing studies. Furthermore, composites of metal oxides-rGO in morphologies other than NFs are not discussed.

2.1. RGO-Loaded Metal Oxides Gas Sensors

2.1.1. rGO-Loaded ZnO NFs

Zinc oxide (ZnO) is one of the most common metal oxides in the gas sensing area because of its unique properties, such as n-type conductivity, low toxicity, ease of synthesis, high availability, good thermal stability, and high mobility of electrons [56,57]. Abideen et al. [58] prepared rGO-loaded ZnO NFs for H_2 gas sensing investigations. At 400 °C, the sensor exhibited an exceptionally strong response (R_a/R_g) of 2542 to 10 ppm H_2 gas. The presence of rGO and a semiconductor (ZnO)-to metal (Zn) transition in a H_2 atmosphere were the main reasons behind the enhanced response to H_2 gas. They suggested that ZnO could be converted to metallic Zn in the presence of H_2 gas because of the high-sensing temperature. Owing to the differences in the work functions of rGO, ZnO, and Zn, at equilibrium, potential barriers were generated at both rGO/Zn and Zn/ZnO interfaces. ZnO was more n-type because of the flow of electrons from the Zn layer to ZnO. Accordingly, high resistance modulation occurred, contributing to the sensing signal. In addition, the potential barriers of rGO/Zn prevented the flow of electrons to rGO, which acted as a source of resistance modulation in the presence of H_2 gas.

In another similar investigation, Abideen et al. reported the effects of the rGO-loading (0.04, 0.11, 0.17, 0.44, 0.77, and 1.04 wt.%) on the NO_2 sensing response of ZnO NFs [59]. Figure 5a,b shows SEM and TEM images of 0.44 wt.% rGO-loaded ZnO NFs, respectively.

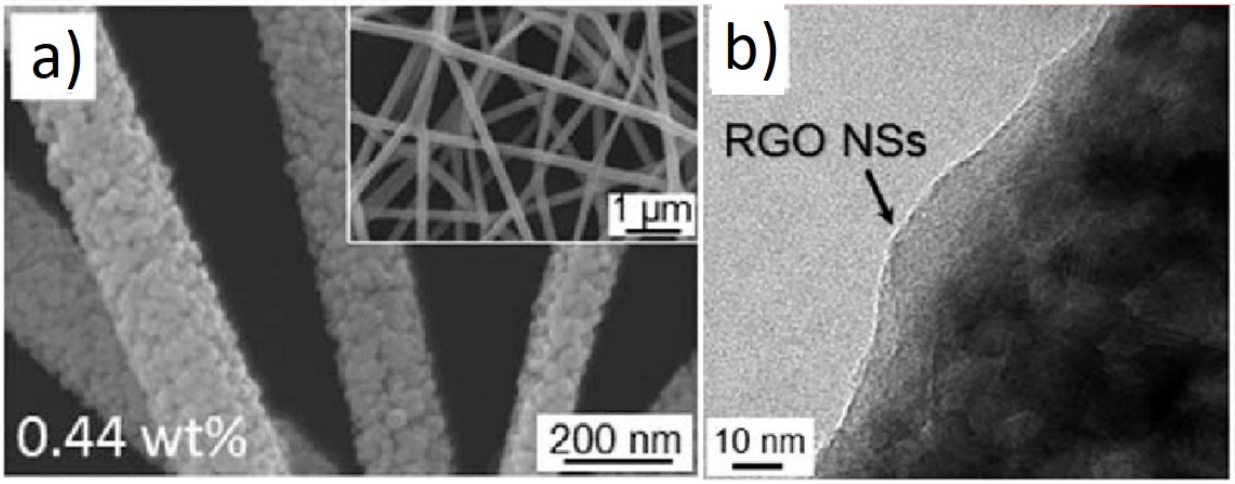

Figure 5. (**a**) SEM image and (**b**) TEM image of 0.44 wt.% rGO-loaded ZnO NFs [59].

Among rGO-loaded ZnO NF gas sensors, the sensor with a 0.44 wt.% rGO-loading showed an enhanced response to NO_2 gas. The sensor showed a response (R_a/R_g) of ~123 to 5 ppm NO_2 gas at 400 °C.The boundaries between the nanograins acted as a source of resistance modulation caused by the generation of potential barriers resulting from oxygen adsorption. After introducing NO_2 gas, the height of the potential barriers increased across the grain boundaries, leading to the sensor signal (Figure 6a).

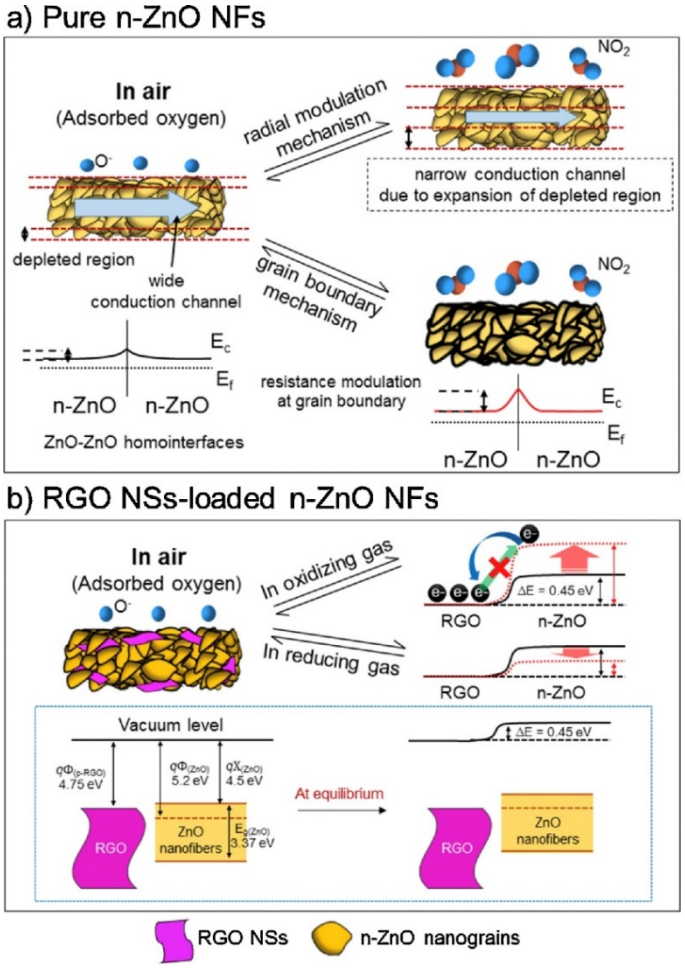

Figure 6. NO_2 gas sensing mechanism of (**a**) ZnO NFs and (**b**) rGO-loaded ZnO NFs [59].

In the rGO/ZnO heterojunctions, Ohmic contact was generated (Figure 6b), acting as a non-rectifying barrier to charge transfer, which affected the sensing behavior. In a NO_2 atmosphere, the resistance of the gas sensor was increased because of the abstraction of more electrons. In addition, discretely distributed rGO nanosheets, which had a high surface area, played a catalytic role on NO_2gas molecules. Other contributions were the presence of defects in rGO, which were favorable sites for the adsorption of gases.

Abideen et al. synthesized rGO-loaded ZnO NFs functionalized by Au and Pd NPs, as shown in Figure 7 [60]. Figure 8a–c shows typical TEM images of rGO nanosheets, ZnO NFs and Au-decorated ZnO NFs, respectively. At 400 °C, the sensors functionalized with Au and Pd showed an enhanced gas response towards CO and C_6H_6 gases, respectively. Owing to the formation of ZnO/rGO heterojunctions, the electron depletion layer was wider in the ZnO NFs. Upon exposure to reducing gases, they interacted with oxygen species and liberated electrons, resulting in increased sensor conductivity, contributing to the sensing signal.

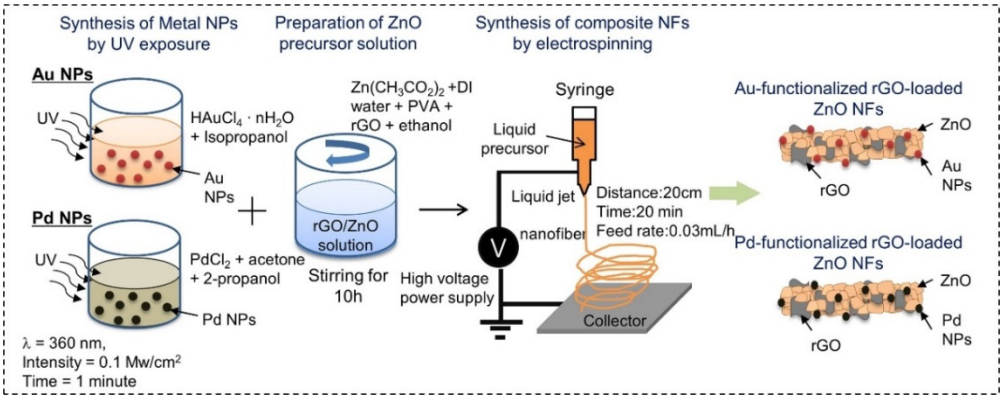

Figure 7. Preparation of Au and Pd-decorated rGO-loaded ZnO NFs [60].

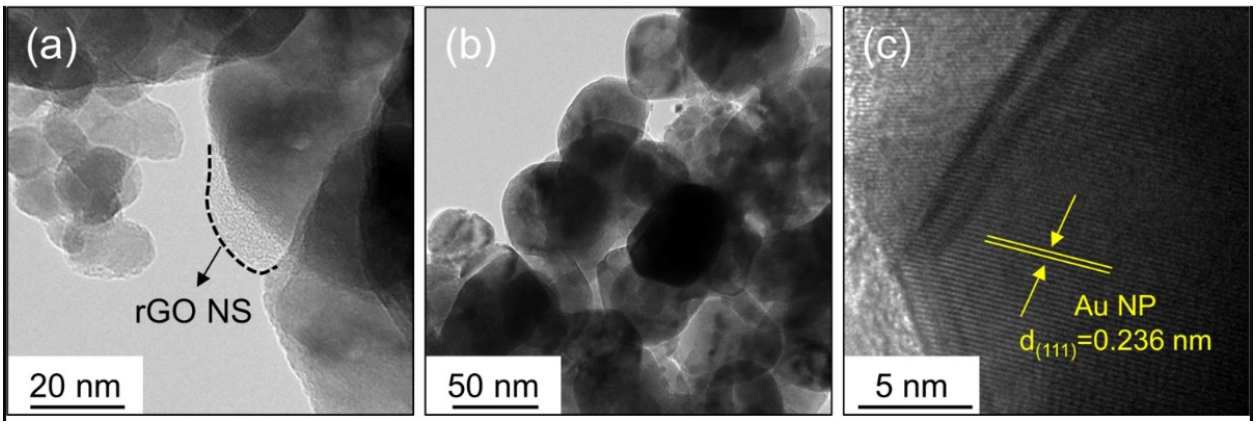

Figure 8. (**a**)TEM imageof Au-functionalized rGO-loaded ZnO NF. (**b**) TEM image of a ZnO NF. (**c**) Lattice-resolved TEM image of Au-functionalized rGO-loaded ZnO NF [60].

rGO has a high surface area, many defects and functional groups, and a different work function than ZnO. These factors contributed to the sensing enhancement. The effects of noble metals were considered. In the case of electronic sensitization, oxidized Pd (PdO), which initially took electrons from ZnO, was reduced in the presence of C_6H_6. Accordingly, the space charge layer was relaxed by the return of electrons to the ZnO. In chemical sensitization, Au and Pd NPs acted as catalytic metals. The incoming oxygen species were adsorbed on the surface of Au or Pd, leading to the dissociation of oxygen and subsequent spillover to neighboring ZnO. This increased the initial width of the electron depletion layers, which acted as a source of resistance modulation in the presence of the target gases. Furthermore, Schottky barriers were formed in the interfaces between Au/ZnO and Pd/ZnO (Figure 9). The width of the electron depletion layer decreased because of the flow of electrons from ZnO to metal. Moreover, the width of the electron depletion layer decreased by subsequent interaction of reducing gases and the liberation of electrons, causing a large change in resistance of the gas sensor.

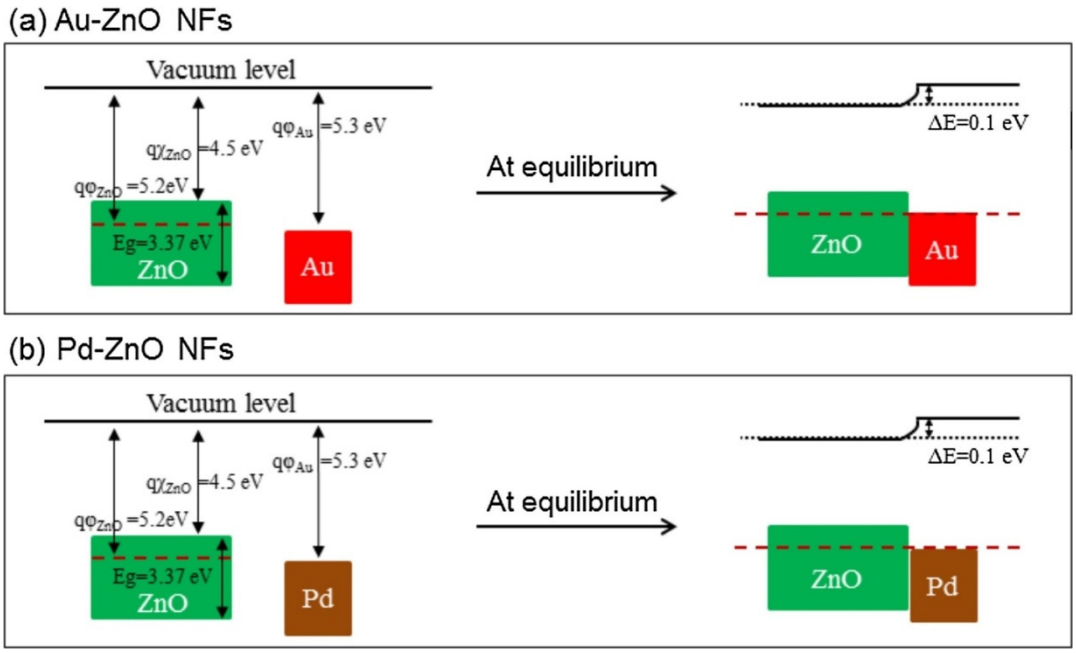

Figure 9. Energy band levelsof (**a**) Au-ZnO and (**b**) Pd-ZnO [60].

The good selectivity of the Au-functionalized gas sensor to CO was attributed to the low (1.20 eV) oxidation barrier of CO on Au and the strong interaction of Au with CO gas. In addition, strong adsorption of C_6H_6 on Pd resulted in the strong response of the Pd-functionalized gas sensor to benzene.

2.1.2. rGO-Loaded SnO_2 NFs

SnO_2 is among the most popular metal oxides for sensing studies because of its high stability, favorable bandgap, low price, and good intrinsic sensing properties [61,62]. Lee et al. [63] examined the effects of rGO-loadings (0.04–1.04 wt.%) on the NO_2 gas sensing properties of SnO_2 NFs produced by electrospinning. The sensor with 0.44 wt.% rGO exhibited the highest resistance and the strongest response (R_a/R_g) of ~100 to 5 ppm NO_2 gas at 200 °C. The pristine sensors showed a change in resistance due to the grain boundary mechanism and radial modulation, as shown in Figure 10a. For rGO-loaded sensors (Figure 10b), p-n heterojunctions were formed, generating potential barriers to the flow of electrons. The heights of these barriers were changed in the target gas atmosphere, resulting in sensing signal generation.

Hollow NFs are also interesting morphologies for gas sensing studies because of their higher surface areas that can interact with gas species [64]. For example, a BET surface area of hollow SnO_2NFs composited with GO was reported to be 33.4m^2/g. In this regard, Li et al. [65] investigated rGO-loaded SnO_2 NFs for gas sensing studies. Figure 11 shows typical SEM and TEM images of rGO-loaded SnO_2 NFs.

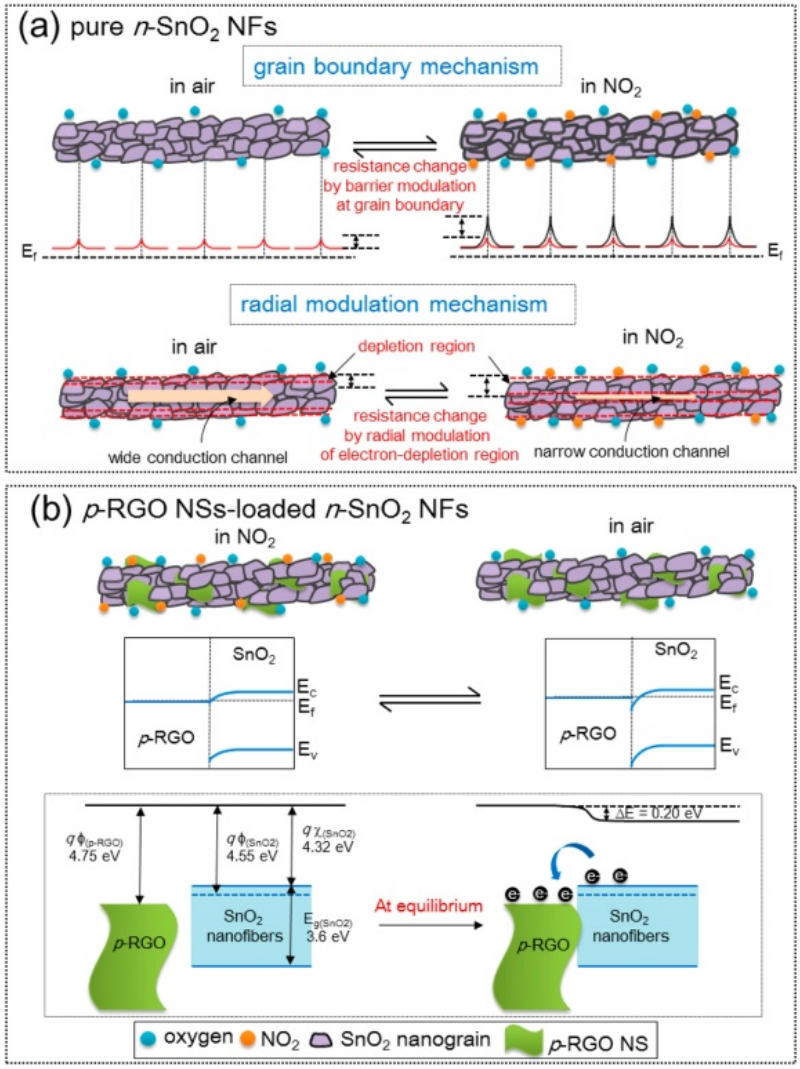

Figure 10. NO_2 sensing mechanism in (**a**) SnO_2 NFs and (**b**) rGO-loaded SnO_2 NFs [63].

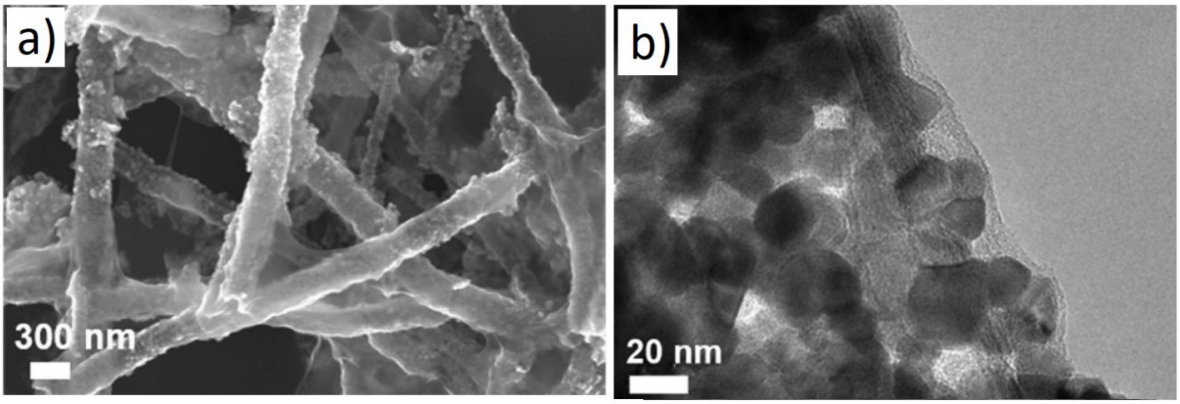

Figure 11. (**a**) SEM image and (**b**) TEM image of rGO-loaded SnO_2 hollow NFs [65].

p-n heterojunctions were formed between the connections owing to the intimate contact between rGO and SnO_2. (Figure 12a). Under UV illumination (Figure 12b), SnO_2acted as a UV absorber and a collector of generated electrons, whereas rGO acted as a photoelectron acceptor and provided many electron transport pathways. Generated electrons,

as a result of UV illumination, can be adsorbed by oxygen species. The holes generated can be combined with chemisorbed oxygen, resulting in the desorption of oxygen. Thus, equilibrium is achieved under UV light. The best response could be achieved by tuning the UV light intensity. Oxidizing gases, such as NO_2, can abstract electrons from the surface of the gas sensor. Compared to the dark condition, many more photoelectrons are captured by NO_2 gas, resulting in a stronger response to NO_2 gas. The strongest response was obtained under a 97 mW/cm^2 UV light intensity, which indicated a response of ~100% ($\Delta R/R_a \times 100$) to 5 ppm NO_2 at room temperature.

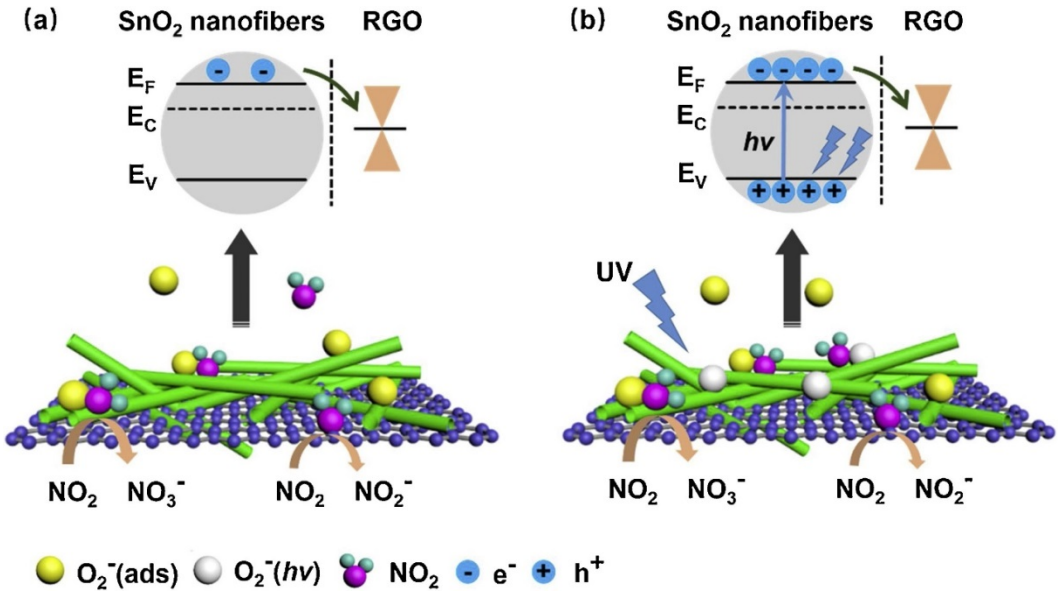

Figure 12. The sensing mechanism of rGO-loaded SnO_2NFs to NO_2(**a**) in the dark and (**b**) UV illumination [65].

Choi et al. [66] prepared 0.01 and 5 wt.% rGO-loaded SnO_2 NFs for sensing studies. In the 0.01 wt.% rGO-loaded sensor, the electrical transport and sensing characteristics of the sensor were dominated by the SnO_2 NFs, which showed an enhanced gas response to H_2S. In contrast, in the sensor with 5 wt.% rGO, the rGO NSs showed an enhanced response to acetone. The 0.01 wt.% rGO NS-loaded SnO_2 NFs showed a response (R_a/R_g) of 33.7 to 5 ppm H_2S at 200 °C. On the other hand, the 5 wt.% rGO-loaded sensor showed a response of 10.4 to 5 ppm acetone at 350 °C. Accordingly, the selectivity of the gas sensor towards H_2S or acetone could be tuned by changing the amount of rGO.

Kim et al. [67] fabricated Pt or Pd rGO-co-loaded SnO_2 NFs for sensing purposes. The sensors sensitized with Pt showed an enhanced gas response to toluene, while the sensor with Pd showed an improved response to benzene. Figure 13 shows the sensing mechanism. rGO plays a role in the formation of heterojunctions with SnO_2, where electrons from SnO_2 migrate to rGO, leading to an expansion of the electron depletion layer of SnO_2 and a change in the width of the electron depletion layer in the presence of target gases, which greatly affect the response to gases. The sensing enhancement of the Pt-functionalized sensor was attributed partially to the H_2 dissociation of gases. Upon dissociation, C_7H_8 can generate more H_2 molecules. Thus, Pt dissociated C_7H_8 more effectively than the remaining gases. Furthermore, the methyl group (-CH_3) on toluene made it easier to adsorb on the Pt surface. Regarding the Pd-functionalized gas sensor, the adsorption energy of C_6H_6/Pd (1.35 eV) was lower than that of C_6H_6/Pt (1.49 eV); thus, the Pd-functionalized gas sensor showed an enhanced response to C_6H_6 compared to C_7H_8 gas.

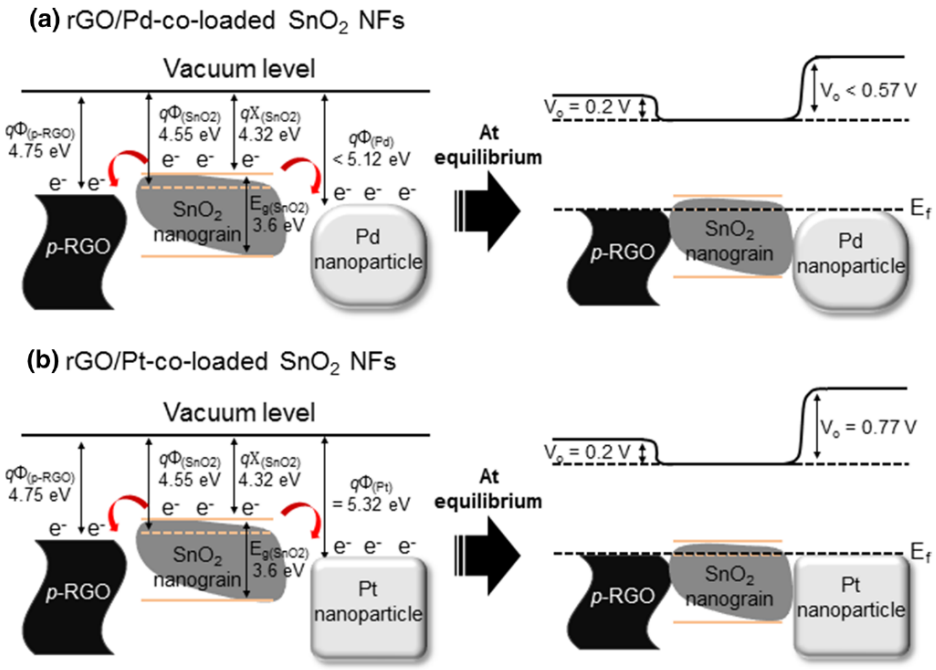

Figure 13. Energy band of (**a**) rGO, SnO_2 Pd, and (**b**) rGO, SnO_2 Pt [67].

2.1.3. rGO-Loaded α-Fe_2O_3 NFs

n-Type α-Fe_2O_3 is one of the most popular oxides, with many excellent features, such as low cost and facile preparation [68]. In that study, 0.5, 1.0, and 3.0wt.% rGO-loaded α-Fe_2O_3 NFs with approximate diameters of 100 nm were prepared using an electrospinning technique. The response of the optimal gas sensor, namely 1wt.% rGO/α-Fe_2O_3NFs at 375 °C to 100ppm acetone was approximately 8.9, which was approximately 4.5 times higher than the pure α-Fe_2O_3gas sensor [69]. The resistance of the composite sensors was lower than that of the pristine sensor, and the sensors with larger amounts of rGO showed lower conductivity. Ohmic contacts were generated because of the formation of rGO-Fe_2O_3 heterojunctions, which contributed to the sensing signal. Furthermore, defects and functional groups in rGO provided strong adsorption sites for gas molecules. In addition, the spaces between the layers of rGO nanosheets acted as an effective gas diffusion channel, which also provided more adsorption sites for gas molecules. When the amount of rGO was 3 wt.%, the surface of Fe_2O_3 was covered further with rGO, resulting in a significant decrease in the number of gas adsorption sites of α-Fe_2O_3. Thus, acetone gas reacted mainly with rGO rather than α-Fe_2O_3NFs, leading to a low response.

Hoang et al. [70] prepared rGO-loaded (0–1.5wt.%) α-Fe_2O_3 NFs for sensing studies. The 1 wt.% rGO loaded sensor showed a strong response (R_a/R_g) of ~9.2 to 1ppm H_2S gas at 350 °C. On the other hand, when rGO was increased, rGO nanosheets were dominant for the electron pathways, which decreased the overall sensor resistance, causing a weaker sensor response. The formation of rGO/Fe_2O_3 heterojunctions (Figure 14), high surface area resulting from the NFs, and strong adsorption sites, such as oxygen functional groups and structural defects, also enhanced the sensor response.

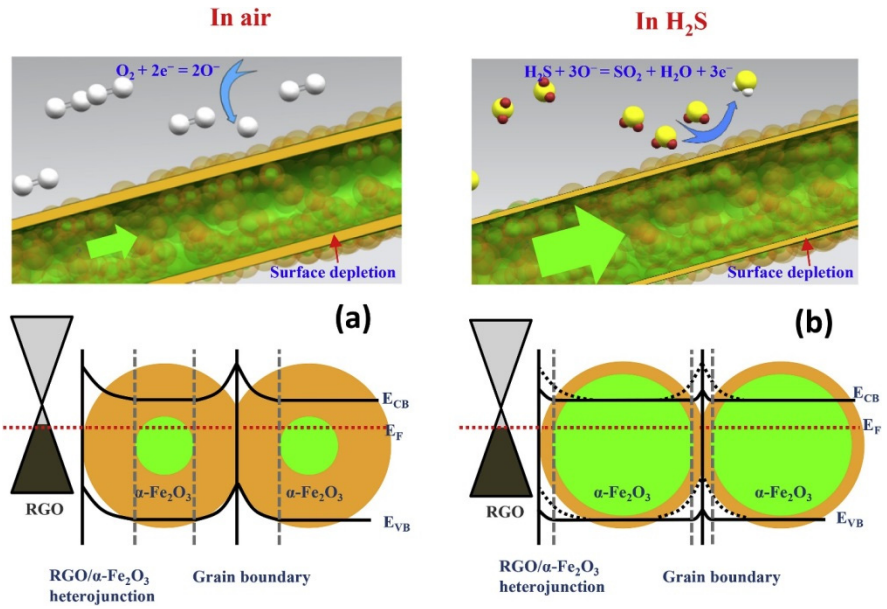

Figure 14. Schematic diagram of H_2S sensing mechanisms of α-Fe_2O_3 NFs and rGO-loaded Fe_2O_3 NFs in (**a**) air and in (**b**) H_2S gas [70].

2.1.4. rGO-Loaded In_2O_3 NFs

As a semiconducting metal oxide, In_2O_3 (E_g = 3.6 eV) is used for sensing studies [71]. On the other hand, pristine In_2O_3 NFs show high resistance at room temperature because of the low mobility of electrons. A good strategy to overcome this problem is to form p-n heterojunctions and increase the overall sensing performance [72,73]. $NH_3$is a highly reactive gas that harms the global greenhouse balance. Furthermore, it can be regarded as a biomarker of the human breath to diagnose lung diseases. Hence, the precise sensing of NH_3gas is necessary [74]. Andre et al. synthesized rGO-loaded In_2O_3 NFs for gas sensing applications [75]. Figure 15 shows TEM analyses of rGO-loaded In_2O_3 NFs.

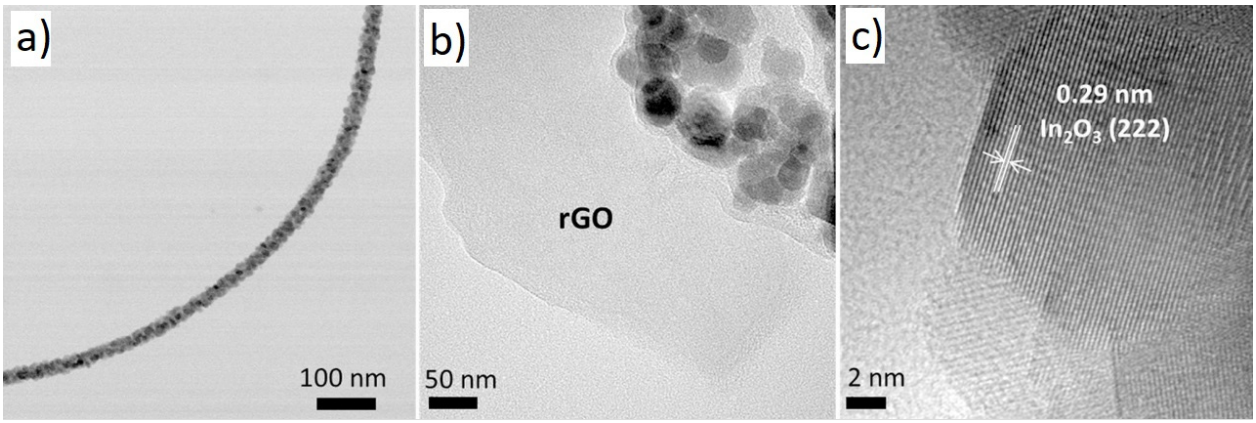

Figure 15. (**a**) Typical TEM image of rGO-loaded In_2O_3 NF. (**b**) TEM image showing rGO and (**c**) High-resolution TEM showing fringe of In_2O_3 [75].

At room temperature, the sensor showed a response of 23.36 to 15 ppm NH_3 gas. p-n heterojunctions of rGO-In_2O_3 were formed in the air upon intimate contact and exposure to NH_3 gas; the electrons released greatly modulated the height of these potential barriers, resulting in the appearance of the sensing signal. Other factors that contributed to the sensing signal were the increase in surface area due to the presence of rGO nanosheets and the synergistic effect between the In_2O_3 structure and rGO nanosheets, which formed a

three-dimensional interconnected morphology, facilitating the gas accessibility depth parts of the sensing layer.

Yan et al. [76] fabricated rGO-loaded In_2O_3 NFs by an electrospinning technique. The sensor with 2.2 wt.% rGO showed an enhanced gas response of 43 to 5 ppm NO_2 gas at 50 °C. Figure 16a,b show the sensing mechanism for the pristine and rGO-loaded gas sensors, respectively. Several contributions were mentioned to explain the sensing mechanism in rGO-loaded In_2O_3 NFs. First, rGO with a high surface area and defects and functional groups provided many adsorption sites for incoming NO_2 gas molecules. Furthermore, potential barriers were formed due to the formation of rGO-In_2O_3 heterojunctions, and the width and height of these barriers were modified upon exposure to NO_2 gas, which changed the resistance of the gas sensor. On the other hand, the amount of rGO was not optimized in the fabricated sensor.

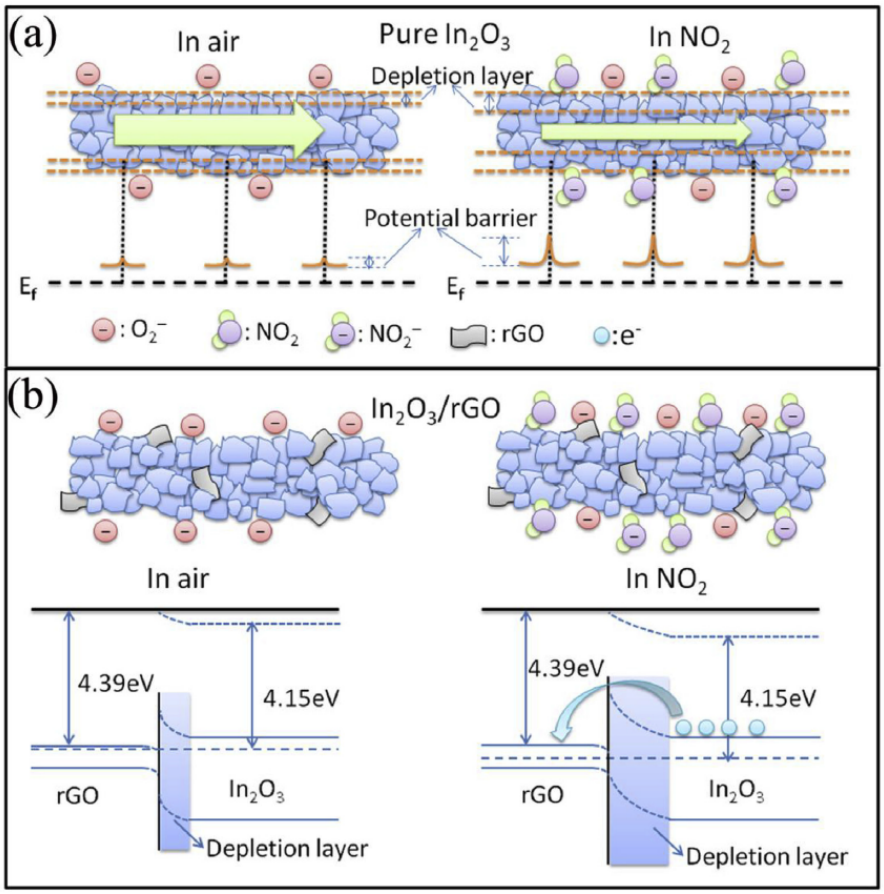

Figure 16. Gas sensing mechanism in (**a**) pristine In_2O_3 (**b**) rGO-loaded In_2O_3 [76].

2.1.5. rGO-Loaded Co_3O_4 NFs

Co_3O_4 is a p-type (E_g = 1.6–2.2 eV) semiconductor and is used for sensing different gases [77–79]. Feng et al. [80] synthesized the rGO-loaded Co_3O_4NFs using the electrospinning technique. At room temperature, the rGO-loaded sensor showed a 10-fold stronger response to NH_3 than the pristine gas sensor. Ammonia is an electron donor gas that donates electrons to rGO upon adsorption. Therefore, the resistance of the gas sensor was increased. The rGO nanosheets interacted with the $Co_3O_4$to form Co-C bonds and therefore were polarized. Thus, the interaction with NH_3, which had one lone pair of electrons, was stronger. The good selectivity was attributed to the different adsorption ability of different gases. Furthermore, NH_3 is more polar than other tested gases, leading to better interactions with the sensing layer.

2.1.6. rGO-Loaded CuO NFs

CuO is a p-type metal oxide for H_2S sensing, even for sub-ppb detection [81]. This is due mainly to the conversion of semiconducting CuO to CuS with metallic-like conductivity [82,83]. Kim et al. [84] used rGO (0.05–1.5 wt.%)-loaded CuO NFs for H_2S gas sensing. The sensor with 0.5 wt.% rGO exhibited the maximum response of 1.95 to 10 ppm H_2S at 300 °C. Figure 17 presents the sensing mechanism. Upon intimate contact between rGO and CuO, heterojunctions were formed, increasing the resistance of the gas sensor. In the H_2S gas atmosphere, CuO was transformed into the CuS phase according to the following reaction:

$$CuO(s) + H_2S(g) \rightarrow CuS\ (s) + H_2O(g) \quad (1)$$

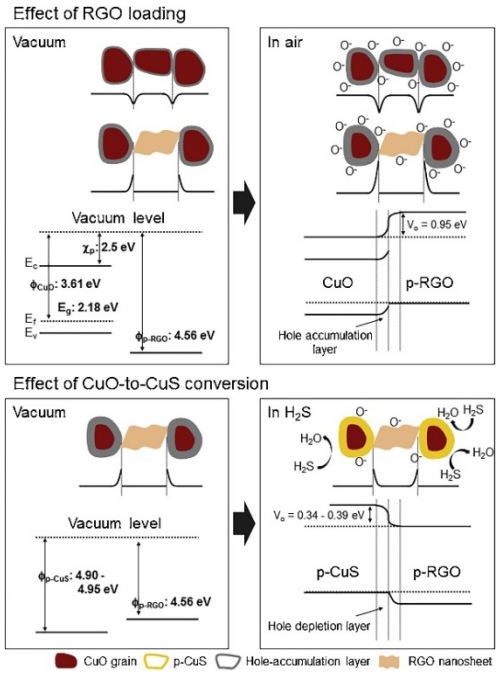

Figure 17. (upper part) Formation of rGO-CuO heterojunctions (lower part) conversion of CuO to CuS conversion [79].

Accordingly, the CuS with metallic conductivity was formed, which led to a significant change in the potential barrier height and decreased the hole accumulation layer, contributing to the sensing signal. rGO nanosheets were separated by CuO crystals, and there was no direct contact among the rGO nanosheets. For small amounts of rGO, the current flowing through CuO was blocked by the presence of discrete rGOs, which acted as a source of modulation. On the other hand, for a high content (>0.5 wt.%) of rGO, the rGO nanosheets provided additional paths for current flow, leading to a higher conduction path along rGO, which reduced the initial resistance and the response of the sensor. The promising roles of rGO nanosheets were also attributed to defects and oxygen functional groups on rGO, which provided many adsorption sites for H_2S gas molecules. Furthermore, with the high surface area of rGO and spillover effect of rGO, H_2S molecules were dissociated on rGO and spilled over to CuO crystals, leading to an increase in the gas response.

2.1.7. rGO-Loaded $ZnFe_2O_4$ NFs

Spinel $ZnFe_2O_4$ (ZFO) is an n-type metal oxide with a normal spinel structure [85] that has gained considerable attention for the detection of gases [86]. Hoang et al. [87] synthesized rGO-loaded ZFO NFs (50–100 nm) for H_2S gas sensing applications. The sensor showed a response of 147 to 1 ppm of H_2S gas at 350 °C. Figure 18 shows the mechanism of gas detection. Electrons from rGO were transferred to ZFO owing to different work

functions, forming heterojunctions on the rGO-ZFO interfaces. Furthermore, potential barriers were formed along the grain boundaries of ZFO due to the adsorption of oxygen molecules. Upon the introduction of H_2S gas, the electrons generated from the interaction of H_2S with oxygen molecules, returned to the surface of the gas sensor, decreasing the barrier height, leading to the sensing signal.

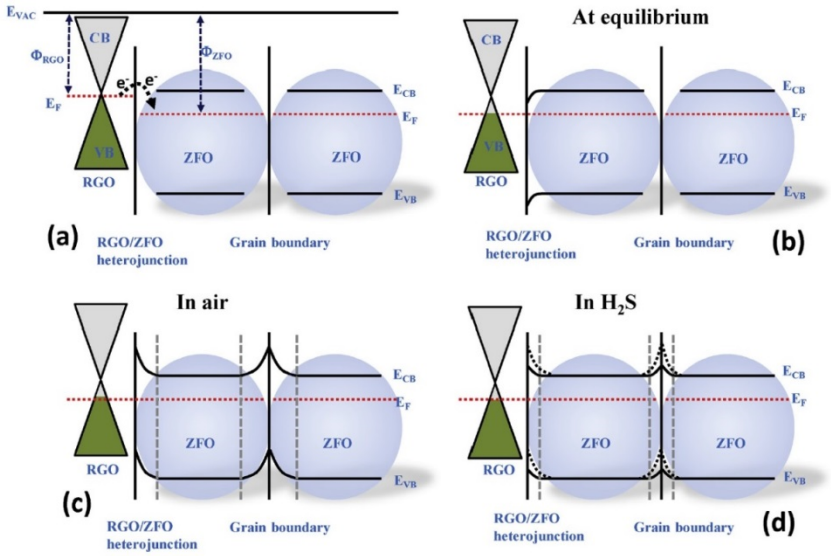

Figure 18. Band energy levels of (**a**) rGO and ZFO, (**b**) at equilibrium, (**c**) in air, and (**d**) in H_2S gas [82].

Table 1 lists the gas sensing characteristics of rGO-loaded metal oxide NFs reported in literature. Different oxidizing (NO_2) and reducing (C_6H_6, H_2, CO, H_2S, C_3H_6O, and C_7H_8) gases, have been successfully detected by these gas sensors. The sensing temperatures ranging from room temperature up to 400 °C have been reported. This demonstrates the possibility of a high sensing temperature of rGO-loaded gas sensors. In some cases, such as Ref. [58], a very high response to target gas can be obtained. Finally, in some cases, high responses to low concentrations of gases have been reported. Overall, the data in Table 1 shows the promising effects of rGO to be used along with metal oxide NFs for gas sensing studies.

Table 1. Gas sensing characteristics of rGO-loaded metal oxide NFs.

Sensing Material	Target Gas	Conc. (ppm)	Response (R_a/R_g)	T (°C)	Ref.
rGO-loaded ZnO NFs	H_2	10	2542	400	[58]
rGO-loaded ZnO NFs	NO_2	5	123	400	[59]
Au/rGO-loaded ZnO NFs	CO	5	35.8	400	[60]
Pd/rGO-loaded ZnO NFs	C_6H_6	5	22.8	400	[60]
0.44 wt.% rGO-loaded SnO_2 NFs	NO_2	5	100	200	[63]
rGO-loaded-SnO_2 NFs under UV light	NO_2	5	100%($\Delta R/R_a \times 100$)	25	[65]
0.01 wt.% rGO-loaded-SnO_2 NFs	H_2S	5	34	200	[66]
5 wt.% rGO-loaded-SnO_2 NFs	C_3H_6O	5	15	350	[66]
rGO/Pd co-loaded SnO_2 NFs	C_6H_6	5	12.3	200	[67]
rGO/Pt co-loaded SnO_2 NFs	C_7H_8	5	16	200	[67]
1 wt.% rGO-loaded Fe_2O_3 NFs	C_3H_6O	100	8.9	375	[69]
1 wt.% rGO-loaded Fe_2O_3 NFs	H_2S	1	9.2	350	[70]
rGO-loaded In_2O_3 NFs	NH_3	15	23.37	25	[75]
2.2 wt.% rGO-loaded In_2O_3 NFs	NO_2	5	43	50	[76]
1wt.% rGO–Co_3O_4NFs	NH_3	50	53.6%($\Delta R/R_a$) × 100	25	[80]
0.5 wt.% rGO-loaded CuO NFs	H_2S	10	1.95	300	[84]
rGO-loaded $ZnFe_2O_4$ NFs	H_2S	1	147	350	[87]

Also, Table 2 summarizes precursors, NF diameter, surface area and porosity of different rGO-loaded NF gas sensors reported in the literature. In all cases, initially, a viscous solution of precursor materials was prepared and then it was loaded into a syringe and subsequently NFs were produced by electrospinning process. It should be noted that in most cases, rGO was reduced from the synthesized GO (via Hummers method). In most cases, the surface area is not mentioned, but it could reach to 78.57 m^2/g. In addition, in most cases the NFs with different diameters and mesoporous nature can be obtained by electrospinning.

Table 2. Precursors, NF diameter, surface area and porosity nature of rGO-loaded NF gas sensors reported in literature.

Sensing Material	Precursors	NF Diameter (nm)	Surface Area (m^2/g)	Porosity Type	Ref.
rGO-loaded ZnO NFs	Zinc acetate, PVA	190	NA	NA	[58]
rGO-loaded ZnO NFs	Zinc acetate, polyvinyl alcohol (PVA)	~150	NA	NA	[59]
Au and Pd/rGO-loaded ZnO NFs	Zinc acetate, PVA, $HAuCl_4 \cdot nH_2O$, $PdCl_2$	~200	NA	Mesoporous	[60]
0.44 wt.% rGO-loaded SnO_2 NFs	$SnCl_2.2H_2O$, polyvinyl acetate (PVAc)	~180	7.0574	Mesoporous	[63]
rGO-loaded-SnO_2 NFs under UV light	$SnCl_2.2H_2O$, PVP, dimethyl formamide (DMF)	80–250	NA	NA	[65]
0.01 wt.% rGO-loaded-SnO_2 NFs	PVP, polymethylmethacrylate (PMMA) + tin(IV) acetate, acetic acid	370	NA	NA	[66]
rGO/Pt and Pd co-loaded SnO_2 NFs	$SnCl_2.2H_2O$, PVAc, $PdCl_2$, $H_2PtCl_6.nH_2O$, DMF	NA	NA	Mesoporous	[67]
1 wt.% rGO-loaded Fe_2O_3 NFs	Ferric acetylacetonte PVP	100	NA	NA	[69]
1 wt.% rGO-loaded Fe_2O_3 NFs	PVA, $Fe(NO_3)_3.9H_2O$	50–100	NA	NA	[70]
rGO-loaded In_2O_3 NFs	$InCl_3$, PVP, Monomethylamine (MMA), Trimethylamine (TMA), Triethylamine (TEA), and N,N-Dimethylformamide (DMF)	50	NA	Mesoporous	[75]
2.2 wt.% rGO-loaded In_2O_3 NFs	PVP, DMF and $(In(NO_3)_3 \cdot 4.5H_2O$	76	39.82	Mesoporous	[76]
1wt.% rGO–Co_3O_4NFs	$Co(NO_3)_2 \cdot 6H_2O$, PVP, Ethanol	200–300	78.57	Mesoporous	[80]
0.5 wt.% rGO-loaded CuO NFs	PVA, $(Cu\ (CH_3CO_2)_2)$	~50	NA	NA	[84]
rGO-loaded $ZnFe_2O_4$ NFs	$Zn(CH_3COO)_2 \cdot 2H_2O$, $Fe(NO_3)_3 \cdot 9H_2O$ and PVA	50–100	NA	Mesoporous	[87]

NA: not available.

3. Conclusions and Outlook

This review discussed various aspects of the sensing mechanisms of rGO-loaded metal oxide NFs gas sensors. Different metal oxides, such as ZnO, SnO_2, Co_3O_4, CuO, In_2O_3, and other metal oxides, were used in combination with rGO for gas sensing applications. Metal oxide NFs with a high surface area, resulting from long and continuous morphology of NFs, produced by electrospinning, are among the most popular choices for gas sensors. Furthermore, as shown in Figure 1, nanograins on the surface of NFs, can increase the surface area of NFs and act as a high resistance source for the gas sensors. Pristine rGO gas sensors generally show weaker sensing properties than metal oxides because of the long response time and recovery time, as well as the lower response. When loaded on metal oxides, rGO nanosheets can increase the overall sensing surface and adsorption sites, which leads to the generation of p-n or p-p heterojunctions with metal oxides and modulate the resistances of the gas sensors. Furthermore, defects in rGO, such as oxygen vacancies and functional groups, can provide strong adsorption sites for target gases. Generally, there is an optimal amount of rGO that can give the strongest gas response. When the amount of rGO is higher than the optimal value, the main current can pass from rGO, which leads to a weaker response. In addition, for larger amounts of rGO nanosheets, some agglomeration may occur, resulting in a weaker response of the gas sensor. There are some strategies, such as functionalization with noble metals, to increase the overall sensing performance of rGO-loaded metal oxide NFs. Therefore, rGO-noble metal co-loaded metal oxides can be quite effective for sensing studies. Further advances can help load rGO nanosheets on

metal oxide composite NFs. For example, p-n heterojunctions between different metal oxides can be fabricated, and the rGO loading can increase the sensing performance further.

Author Contributions: conceptualization, H.W.K. and S.S.K.; resources, S.M.M. and A.M.; writing original draft preparation, A.M. and S.M.M.; review and editing, H.W.K. and S.S.K.; supervision, H.W.K. and S.S.K. All authors have read and agreed to the published version of the manuscript.

Funding: This research received no external funding.

Institutional Review Board Statement: Not applicable.

Informed Consent Statement: Not applicable.

Data Availability Statement: Not applicable.

Acknowledgments: This work was supported by INHA UNIVERSITY Research Grant.

Conflicts of Interest: The authors declare no conflict of interest.

References

1. Velmathi, G.; Mohan, S.; Henry, R. Analysis and review of tin oxide-based chemoresistive gas sensor. *IETE Tech. Rev.* **2016**, *33*, 323–331. [CrossRef]
2. Wetchakun, K.; Samerjai, T.; Tamaekong, N.; Liewhiran, C.; Siriwong, C.; Kruefu, V.; Wisitsoraat, A.; Tuantranont, A.; Phanichphant, S. Semiconducting metal oxides as sensors for environmentally hazardous gases. *Sens. Actuators B Chem.* **2011**, *160*, 580–591. [CrossRef]
3. Feng, S.; Farha, F.; Li, Q.; Wan, Y.; Xu, Y.; Zhang, T.; Ning, H. Review on smart gas sensing technology. *Sensors* **2019**, *19*, 3760. [CrossRef] [PubMed]
4. Majhi, S.M.; Mirzaei, A.; Kim, H.W.; Kim, S.S.; Kim, T.W. Recent advances in energy-saving chemiresistive gas sensors: A review. *Nano Energy* **2021**, *79*, 105369. [CrossRef] [PubMed]
5. Mirzaei, A.; Kim, J.-H.; Kim, H.W.; Kim, S.S. Resistive-based gas sensors for detection of benzene, toluene and xylene (btx) gases: A review. *J. Mater. Chem. C* **2018**, *6*, 4342–4370. [CrossRef]
6. Nazemi, H.; Joseph, A.; Park, J.; Emadi, A. Advanced micro- and nano-gas sensor technology: A review. *Sensors* **2019**, *19*, 1285. [CrossRef]
7. Wang, J.; Shen, H.; Xia, Y.; Komarneni, S. Light-activated room-temperature gas sensors based on metal oxide nanostructures: A review on recent advances. *Ceram. Inter.* **2020**. Corrected Proof. [CrossRef]
8. Miller, D.R.; Akbar, S.A.; Morris, P.A. Nanoscale metal oxide-based heterojunctions for gas sensing: A review. *Sens. Actuators B Chem.* **2014**, *204*, 250–272. [CrossRef]
9. Singhal, A.V.; Charaya, H.; Lahiri, I. Noble metal decorated graphene-based gas sensors and their fabrication: A review. *Crit. Rev. Solid State Mater. Sci.* **2017**, *42*, 499–526. [CrossRef]
10. Kim, J.-H.; Kim, J.-Y.; Lee, J.-H.; Mirzaei, A.; Kim, H.W.; Hishita, S.; Kim, S.S. Indium-implantation-induced enhancement of gas sensing behaviors of SnO_2 nanowires by the formation of homo-core–shell structure. *Sens. Actuators B Chem.* **2020**, *321*, 128475. [CrossRef]
11. Chen, X.; Wong, C.K.Y.; Yuan, C.A.; Zhang, G. Nanowire-based gas sensors. *Sens. Actuators B Chem.* **2013**, *177*, 178–195. [CrossRef]
12. Rezaie, S.; Bafghi, Z.G.; Manavizadeh, N. Carbon-doped zno nanotube-based highly effective hydrogen gas sensor: A first-principles study. *Int. J. Hydrogen Energy* **2020**, *45*, 14174–14182. [CrossRef]
13. Gao, R.; Cheng, X.; Gao, S.; Zhang, X.; Xu, Y.; Zhao, H.; Huo, L. Highly selective detection of saturated vapors of abused drugs by ZnO nanorod bundles gas sensor. *Appl. Surf. Sci.* **2019**, *485*, 266–273. [CrossRef]
14. Suman, P.; Felix, A.; Tuller, H.; Varela, J.; Orlandi, M. Comparative gas sensor response of SnO_2, SnO and Sn_3O_4 nanobelts to SnO_2 and potential interferents. *Sens. Actuators B Chem.* **2015**, *208*, 122–127. [CrossRef]
15. Choi, S.-J.; Kim, I.-D. Recent developments in 2D nanomaterials for chemiresistive-type gas sensors. *Electron. Mater. Lett.* **2018**, *14*, 221–260. [CrossRef]
16. Lee, J.-H. Gas sensors using hierarchical and hollow oxide nanostructures: Overview. *Sens. Actuators B Chem.* **2009**, *140*, 319–336. [CrossRef]
17. Korotcenkov, G.; Cho, B.K. Porous semiconductors: Advanced material for gas sensor applications. *Crit. Rev. Solid State Mater. Sci.* **2010**, *35*, 1–37. [CrossRef]
18. Lu, Z.; Zhou, Q.; Wei, Z.; Xu, L.; Peng, S.; Zeng, W. Synthesis of hollow nanofibers and application on detecting SF6 decomposing products: A mini review. *Front. Mater.* **2019**, *6*, 183. [CrossRef]
19. Hanh, N.H.; Van Duy, L.; Hung, C.M.; Van Duy, N.; Heo, Y.-W.; Van Hieu, N.; Hoa, N.D. Voc gas sensor based on hollow cubic assembled nanocrystal Zn_2SnO_4 for breath analysis. *Sens. Actuators A Phys.* **2020**, *302*, 111834. [CrossRef]
20. Kim, J.-H.; Mirzaei, A.; Woo Kim, H.; Wu, P.; Kim, S.S. Design of supersensitive and selective zno-nanofiber-based sensors for H_2 gas sensing by electron-beam irradiation. *Sens. Actuators B Chem.* **2019**, *293*, 210–223. [CrossRef]

21. Kim, J.-H.; Lee, J.-H.; Mirzaei, A.; Kim, H.W.; Kim, S.S. Optimization and gas sensing mechanism of n-SnO_2-p-Co_3O_4 composite nanofibers. *Sens. Actuators B Chem.* **2017**, *248*, 500–511. [CrossRef]
22. Aruna, S.T.; Balaji, L.; Kumar, S.S.; Prakash, B.S.J. Electrospinning in solid oxide fuel cells—A review. *Renew. Sustain. Energy Rev.* **2017**, *67*, 673–682. [CrossRef]
23. Phuoc, P.H.; Hung, C.M.; Van Toan, N.; Van Duy, N.; Hoa, N.D.; Van Hieu, N. One-step fabrication of SnO_2 porous nanofiber gas sensors for sub-ppm H_2S detection. *Sens. Actuators A. Phys.* **2020**, *303*, 111722. [CrossRef]
24. Gao, X.; Li, F.; Wang, R.; Zhang, T. A formaldehyde sensor: Significant role of pn heterojunction in gas-sensitive core-shell nanofibers. *Sens. Actuators B Chem.* **2018**, *258*, 1230–1241. [CrossRef]
25. Yoon, J.; Yang, H.S.; Lee, B.S.; Yu, W.R.J.A.M. Recent progress in coaxial electrospinning: New parameters, various structures, and wide applications. *Adv. Mater.* **2018**, *30*, 1704765. [CrossRef] [PubMed]
26. Yu, D.G.; Wang, M.; Li, X.; Liu, X.; Zhu, L.M.; Annie Bligh, S.W. Multifluid electrospinning for the generation of complex nanostructures. *Wiley Interdisciplinary Reviews: Nanomed. Nanobiotechnol.* **2020**, *12*, e1601. [CrossRef] [PubMed]
27. Kishan, A.P.; Cosgriff-Hernandez, E.M. Recent advancements in electrospinning design for tissue engineering applications: A review. *J. Biomed. Mater. Res. Part A* **2017**, *105*, 2892–2905. [CrossRef]
28. Abideen, Z.U.; Kim, J.-H.; Lee, J.-H.; Kim, J.-Y.; Mirzaei, A.; Kim, H.W.; Kim, S.S. Electrospun metal oxide composite nanofibers gas sensors: A review. *J. Korean Ceram. Soc.* **2017**, *54*, 366–379. [CrossRef]
29. Liu, Q.; Zhu, J.; Zhang, L.; Qiu, Y. Recent advances in energy materials by electrospinning. *Renew. Sustain. Energy Rev.* **2018**, *81*, 1825–1858. [CrossRef]
30. Li, X.; Chen, W.; Qian, Q.; Huang, H.; Chen, Y.; Wang, Z.; Chen, Q.; Yang, J.; Li, J.; Mai, Y.-W. Electrospinning-based strategies for battery materials. *Adv. Energy Mater.* **2020**, *11*, 2000845. [CrossRef]
31. Xue, J.; Wu, T.; Dai, Y.; Xia, Y. Electrospinning and electrospun nanofibers: Methods, materials, and applications. *Chem. Rev.* **2019**, *119*, 5298–5415. [CrossRef]
32. Xue, J.; Xie, J.; Liu, W.; Xia, Y. Electrospun nanofibers: New concepts, materials, and applications. *Acc. Chem. Res.* **2017**, *50*, 1976–1987. [CrossRef]
33. Wen, P.; Zong, M.-H.; Linhardt, R.J.; Feng, K.; Wu, H. Electrospinning: A novel nano-encapsulation approach for bioactive compounds. *Trends Food Sci. Technol.* **2017**, *70*, 56–68. [CrossRef]
34. Patil, J.V.; Mali, S.S.; Kamble, A.S.; Hong, C.K.; Kim, J.H.; Patil, P.S. Electrospinning: A versatile technique for making of 1D growth of nanostructured nanofibers and its applications: An experimental approach. *Appl. Surf. Sci.* **2017**, *423*, 641–674. [CrossRef]
35. Li, X.; Yu, J.; Wageh, S.; Al-Ghamdi, A.A.; Xie, J. Graphene in photocatalysis: A review. *Small* **2016**, *12*, 6640–6696. [CrossRef]
36. Rao, C.N.R.; Sood, A.K.; Subrahmanyam, K.S.; Govindaraj, A. Graphene: The new two-dimensional nanomaterial. *Angew. Chem. Int. Ed.* **2009**, *48*, 7752–7777. [CrossRef] [PubMed]
37. Schedin, F.; Geim, A.K.; Morozov, S.V.; Hill, E.; Blake, P.; Katsnelson, M.; Novoselov, K.S. Detection of individual gas molecules adsorbed on graphene. *Nat. Mater.* **2007**, *6*, 652–655. [CrossRef] [PubMed]
38. Wang, X.; You, H.; Liu, F.; Li, M.; Wan, L.; Li, S.; Li, Q.; Xu, Y.; Tian, R.; Yu, Z.; et al. Large-scale synthesis of few-layered graphene using CVD. *Chem. Vap. Depos.* **2009**, *15*, 53–56. [CrossRef]
39. Si, Y.; Samulski, E.T. Synthesis of water soluble graphene. *Nano Lett.* **2008**, *8*, 1679–1682. [CrossRef]
40. Zhang, M.; Bai, L.; Shang, W.; Xie, W.; Ma, H.; Fu, Y.; Fang, D.; Sun, H.; Fan, L.; Han, M.; et al. Facile synthesis of water-soluble, highly fluorescent graphene quantum dots as a robust biological label for stem cells. *J. Mater. Chem.* **2012**, *22*, 7461–7467. [CrossRef]
41. Smith, A.T.; LaChance, A.M.; Zeng, S.; Liu, B.; Sun, L. Synthesis, properties, and applications of graphene oxide/reduced graphene oxide and their nanocomposites. *Nano Mater. Sci.* **2019**, *1*, 31–47. [CrossRef]
42. Gupta Chatterjee, S.; Chatterjee, S.; Ray, A.K.; Chakraborty, A.K. Graphene-metal oxide nanohybrids for toxic gas sensor: A review. *Sens. Actuators B Chem.* **2015**, *221*, 1170–1181. [CrossRef]
43. Kumar, R.; Kaur, A. Chemiresistive gas sensors based on thermally reduced graphene oxide for sensing sulphur dioxide at room temperature. *Diam. Relat. Mater.* **2020**, *109*, 108039. [CrossRef]
44. Toda, K.; Furue, R.; Hayami, S. Recent progress in applications of graphene oxide for gas sensing: A review. *Anal. Chim. Acta* **2015**, *878*, 43–53. [CrossRef] [PubMed]
45. Pendolino, F.; Armata, N. *Graphene Oxide in Environmental Remediation Process*; Springer: Cham, Switzerland, 2017; pp. 5–21.
46. Guex, L.G.; Sacchi, B.; Peuvot, K.F.; Andersson, R.L.; Pourrahimi, A.M.; Ström, V.; Farris, S.; Olsson, R.T. Experimental review: Chemical reduction of graphene oxide (GO) to reduced graphene oxide (rGO) by aqueous chemistry. *Nanoscale* **2017**, *9*, 9562–9571. [CrossRef] [PubMed]
47. Xiao, Y.; Yang, Q.; Wang, Z.; Zhang, R.; Gao, Y.; Sun, P.; Sun, Y.; Lu, G. Improvement of SnO_2 gas sensing performance based on discoid tin oxide modified by reduced graphene oxide. *Sensors Actuators B Chem.* **2016**, *227*, 419–426. [CrossRef]
48. Hummers, W.S.; Offeman, R.E. Preparation of graphitic oxide. *J. Am. Chem. Soc.* **1958**, *80*, 1339. [CrossRef]
49. Brodie, B.C. Hydration behavior and dynamics of water molecules in graphite oxide. *Ann. Chim. Phys.* **1860**, *59*, 466–472.
50. Mohan, V.B.; Lau, K.-T.; Hui, D.; Bhattacharyya, D. Graphene-based materials and their composites: A review on production, applications and product limitations. *Comp. Part B. Eng.* **2018**, *142*, 200–220. [CrossRef]

51. Cui, P.; Lee, J.; Hwang, E.; Lee, H. One-pot reduction of graphene oxide at subzero temperatures. *Chem. Commun.* **2011**, *47*, 12370–12372. [CrossRef]
52. Drmosh, Q.A.; Yamani, Z.H.; Hendi, A.H.; Gondal, M.A.; Moqbel, R.A.; Saleh, T.A.; Khan, M.Y. A novel approach to fabricating a ternary rGO/ZnO/Pt system for high-performance hydrogen sensor at low operating temperatures. *Appl. Surf. Sci.* **2019**, *464*, 616–626. [CrossRef]
53. Park, H.J.; Kim, W.-J.; Lee, H.-K.; Lee, D.-S.; Shin, J.-H.; Jun, Y.; Yun, Y.J. Highly flexible, mechanically stable, and sensitive NO_2 gas sensors based on reduced graphene oxide nanofibrous mesh fabric for flexible electronics. *Sens. Actuators B Chem.* **2018**, *257*, 846–852. [CrossRef]
54. Zou, B.; Gou, Y.; Shen, N.; Xiao, A.; Li, M.; Zhu, L.; Wan, P.; Sun, X. Sulfophenyl-Functionalized reduced graphene oxide networks on electrospun 3D scaffold for ultrasensitive NO_2 Gas Sensor. *Sensors* **2017**, *17*, 2954. [CrossRef] [PubMed]
55. Yuan, W.; Huang, L.; Zhou, Q.; Shi, G. Ultrasensitive and selective nitrogen dioxide sensor based on self-assembled graphene/polymer composite nanofibers. *ACS Appl. Mater. Interfaces* **2014**, *6*, 17003–17008. [CrossRef] [PubMed]
56. Zhu, L.; Zeng, W. Room-temperature gas sensing of ZnO-based gas sensor: A review. *Sens. Actuators A Phys.* **2017**, *267*, 242–261. [CrossRef]
57. Kumar, R.; Al-Dossary, O.; Kumar, G.; Umar, A. Zinc oxide nanostructures for SnO_2 gas–sensor applications: A review. *Nano-Micro Lett.* **2015**, *7*, 97–120. [CrossRef] [PubMed]
58. Abideen, Z.U.; Kim, H.W.; Kim, S.S. An ultra-sensitive hydrogen gas sensor using reduced graphene oxide-loaded ZnO nanofibers. *Chem. Commun.* **2015**, *51*, 15418–15421. [CrossRef]
59. Abideen, Z.U.; Katoch, A.; Kim, J.-H.; Kwon, Y.J.; Kim, H.W.; Kim, S.S. Excellent gas detection of ZnO nanofibers by loading with reduced graphene oxide nanosheets. *Sens. Actuators B Chem.* **2015**, *221*, 1499–1507. [CrossRef]
60. Abideen, Z.U.; Kim, J.-H.; Mirzaei, A.; Kim, H.W.; Kim, S.S. Sensing behavior to ppm-level gases and synergistic sensing mechanism in metal-functionalized rgo-loaded ZnO nanofibers. *Sens. Actuators B Chem.* **2018**, *255*, 1884–1896. [CrossRef]
61. Das, S.; Jayaraman, V. SnO_2: A comprehensive review on structures and gas sensors. *Prog. Mater. Sci.* **2014**, *66*, 112–255. [CrossRef]
62. Yamazoe, N.; Sakai, G.; Shimanoe, K. Oxide semiconductor gas sensors. *J. Catal. Surv. Asia* **2003**, *7*, 63–75. [CrossRef]
63. Lee, J.-H.; Katoch, A.; Choi, S.-W.; Kim, J.-H.; Kim, H.W.; Kim, S.S. Extraordinary improvement of gas-sensing performances in SnO_2 nanofibers due to creation of local p–n heterojunctions by loading reduced graphene oxide nanosheets. *ACS Appl. Mater. Interfaces* **2015**, *7*, 3101–3109. [CrossRef] [PubMed]
64. Wang, D.; Zhang, M.; Chen, Z.; Li, H.; Chen, A.; Wang, X.; Yang, J. Enhanced formaldehyde sensing properties of hollow SnO_2 nanofibers by graphene oxide. *Sens. Actuators B Chem.* **2017**, *250*, 533–542. [CrossRef]
65. Li, W.; Guo, J.; Cai, L.; Qi, W.; Sun, Y.; Xu, J.-L.; Sun, M.; Zhu, H.; Xiang, L.; Xie, D.; et al. UV light irradiation enhanced gas sensor selectivity of NO_2 and SO_2 using rgo functionalized with hollow SnO_2 nanofibers. *Sens. Actuators B Chem.* **2019**, *290*, 443–452. [CrossRef]
66. Choi, S.-J.; Jang, B.-H.; Lee, S.-J.; Min, B.K.; Rothschild, A.; Kim, I.-D. Selective detection of acetone and hydrogen sulfide for the diagnosis of diabetes and halitosis using SnO_2 nanofibers functionalized with reduced graphene oxide nanosheets. *ACS Appl. Mater. Interfaces* **2014**, *6*, 2588–2597. [CrossRef] [PubMed]
67. Kim, J.-H.; Zheng, Y.; Mirzaei, A.; Kim, H.W.; Kim, S.S. Synthesis and selective sensing properties of rgo/metal-coloaded SnO_2 nanofibers. *J. Electron. Mater.* **2017**, *46*, 3531–3541. [CrossRef]
68. Mirzaei, A.; Hashemi, B.; Janghorban, K. A-Fe_2O_3 based nanomaterials as gas sensors. *J. Mater. Sci. Mater. Electron.* **2016**, *27*, 3109–3144. [CrossRef]
69. Guo, L.; Kou, X.; Ding, M.; Wang, C.; Dong, L.; Zhang, H.; Feng, C.; Sun, Y.; Gao, Y.; Sun, P.; et al. Reduced graphene oxide/α-Fe_2O_3 composite nanofibers for application in gas sensors. *Sens. Actuators B Chem.* **2017**, *244*, 233–242. [CrossRef]
70. Van Hoang, N.; Hung, C.M.; Hoa, N.D.; Van Duy, N.; Van Toan, N.; Hong, H.S.; Hong Van, P.T.; Sơn, N.T.; Yoon, S.-G.; Van Hieu, N. Enhanced H_2S gas-sensing performance of α-Fe_2O_3 nanofibers by optimizing process conditions and loading with reduced graphene oxide. *J. Alloys Comp.* **2020**, *826*, 154169. [CrossRef]
71. Kumar, V.; Majhi, S.M.; Kim, K.-H.; Kim, H.W.; Kwon, E.E. Advances in In_2O_3-based materials for the development of hydrogen sulfide sensors. *Chem. Eng. J.* **2021**, *404*, 126472. [CrossRef]
72. Korotcenkov, G.; Boris, I.; Cornet, A.; Rodriguez, J.; Cirera, A.; Golovanov, V.; Lychkovsky, Y.; Karkotsky, G. The influence of additives on gas sensing and structural properties of In_2O_3-based ceramics. *Sens. Actuators B Chem.* **2007**, *120*, 657–664. [CrossRef]
73. Li, C.; Feng, C.; Qu, F.; Liu, J.; Zhu, L.; Lin, Y.; Wang, Y.; Li, F.; Zhou, J.; Ruan, S. Electrospun nanofibers of p-type nio/n-type Zno heterojunction with different nio content and its influence on trimethylamine sensing properties. *Sens. Actuators B Chem.* **2015**, *207*, 90–96. [CrossRef]
74. Kwak, D.; Lei, Y.; Maric, R. Ammonia gas sensors: A comprehensive review. *Talanta* **2019**, *204*, 713–730. [CrossRef]
75. Andre, R.S.; Mercante, L.A.; Facure, M.H.M.; Mattoso, L.H.C.; Correa, D.S. Enhanced and selective ammonia detection using In_2O_3/reduced graphene oxide hybrid nanofibers. *App. Surf. Sci.* **2019**, *473*, 133–140. [CrossRef]
76. Yan, C.; Lu, H.; Gao, J.; Zhang, Y.; Guo, Q.; Ding, H.; Wang, Y.; Wei, F.; Zhu, G.; Yang, Z. Improved NO_2 sensing properties at low temperature using reduced graphene oxide nanosheet–In_2O_3 heterojunction nanofibers. *J. Alloys Comp.* **2018**, *741*, 908–917. [CrossRef]
77. Vetter, S.; Haffer, S.; Wagner, T.; Tiemann, M. Nanostructured Co_3O_4 as a co gas sensor: Temperature-dependent behavior. *Sens. Actuators B Chem.* **2015**, *206*, 133–138. [CrossRef]

78. Wen, Z.; Zhu, L.; Mei, W.; Hu, L.; Li, Y.; Sun, L.; Cai, H.; Ye, Z. Rhombus-shaped Co_3O_4 nanorod arrays for high-performance gas sensor. *Sens. Actuators B Chem.* **2013**, *186*, 172–179. [CrossRef]
79. Li, W.Y.; Xu, L.N.; Chen, J. Co_3O_4 nanomaterials in lithium-ion batteries and gas sensors. *Adv. Funct. Mater.* **2005**, *15*, 851–857. [CrossRef]
80. Feng, Q.; Li, X.; Wang, J.; Gaskov, A.M. Reduced graphene oxide (rGO) encapsulated Co_3O_4 composite nanofibers for highly selective ammonia sensors. *Sens. Actuators B Chem.* **2016**, *222*, 864–870. [CrossRef]
81. Li, D.; Tang, Y.; Ao, D.; Xiang, X.; Wang, S.; Zu, X. Ultra-highly sensitive and selective H_2S gas sensor based on cuo with sub-ppb detection limit. *Int. J. Hydrog. Energy.* **2019**, *44*, 3985–3992. [CrossRef]
82. Mirzaei, A.; Kim, S.S.; Kim, H.W. Resistance-based H_2S gas sensors using metal oxide nanostructures: A review of recent advances. *J. Hazard. Mater.* **2018**, *357*, 314–331. [CrossRef]
83. Wang, X.; Li, S.; Xie, L.; Li, X.; Lin, D.; Zhu, Z. Low-temperature and highly sensitivity h2s gas sensor based on ZnO/CuO composite derived from bimetal metal-organic frameworks. *Ceram. Int.* **2020**, *46*, 15858–15866. [CrossRef]
84. Kim, J.-H.; Mirzaei, A.; Zheng, Y.; Lee, J.-H.; Kim, J.-Y.; Kim, H.W.; Kim, S.S. Enhancement of H_2S sensing performance of p-Cuo nanofibers by loading p-reduced graphene oxide nanosheets. *Sens. Actuators B Chem.* **2019**, *281*, 453–461. [CrossRef]
85. Hill, R.J.; Craig, J.R.; Gibbs, G.V. Systematics of the spinel structure type. *Phys. Chem. Miner.* **1979**, *4*, 317–339. [CrossRef]
86. Yan, Y.; Nizamidin, P.; Turdi, G.; Kari, N.; Yimit, A. Room-temperature H_2S gas sensor based on au-doped $ZnFe_2O_4$ yolk-shell microspheres. *Anal. Sci.* **2017**, *33*, 945–951. [CrossRef] [PubMed]
87. Van Hoang, N.; Hung, C.M.; Hoa, N.D.; Van Duy, N.; Park, I.; Van Hieu, N. Excellent detection of H_2S gas at ppb concentrations using $ZnFe_2O_4$ nanofibers loaded with reduced graphene oxide. *Sens. Actuators B Chem.* **2019**, *282*, 876–884. [CrossRef]